Materials Horizons

ROYAL SOCIETY OF CHEMISTRY

COMMUNICATION

View Article Online
View Journal



Cite this: DOI: 10.1039/d5mh02136g

Received 9th November 2025,
Accepted 5th March 2026

DOI: 10.1039/d5mh02136g

rsc.li/materials-horizons

# Eigenmode steering in spatiotemporal gain–loss acoustic metamaterials

Wai Chun Wong, Gregory J. Chaplain and Jensen Li *

**We present a spatiotemporal gain–loss framework for eigenmode steering in coupled acoustic resonators. A cross-coupled gain–loss coefficient links the gain of one resonator to the intensity of its partner, creating nonlinear feedback that conserves total energy while driving the system toward the eigenmode associated with the eigenvalue having the largest imaginary part—a deterministic eigenmode steering. Spatial gain–loss profiles shape the eigenvalue spectrum and attractor landscape, while temporal modulation governs the transition dynamics. When symmetry prevents direct access to a target eigenmode, controlled spatiotemporal perturbations enable otherwise symmetry-forbidden transitions and accelerate convergence. Within this framework, parity–time ($\mathscr{P}\mathscr{J}$) symmetry appears as a special case, allowing tunable switching between steering and Rabi-like oscillations near the exceptional point. Full-wave simulations of coupled Helmholtz resonators confirm precise and programmable acoustic energy routing, establishing spatiotemporal gain–loss engineering as a route to reconfigurable wave control and analog information processing.**

### New concepts

We introduce a materials framework where spatiotemporal gain–loss coupling serves as a design principle for directing modal evolution. In this approach, cross-coupled feedback between resonators establishes a controllable landscape of eigenmodes, within which temporal modulation acts as the driver for transitions. This enables active navigation of modal dynamics, including controlled switching, accelerated convergence, and access to transitions that are normally restricted by symmetry. Unlike traditional non-Hermitian or parity-time ($\mathscr{P}\mathscr{J}$)-symmetric systems that operate under static configurations, the present concept treats time as an intrinsic design dimension for shaping both modal pathways and stability. The resulting framework connects wave dynamics, feedback control, and material programmability, offering a foundation for reconfigurable metamaterials and adaptive information processing.

## 1 Introduction

Time-varying media are systems whose physical parameters are deliberately modulated in time to control how waves evolve, enabling transitions between different physical states or modes. When the Hamiltonian varies slowly within the adiabatic regime, the system remains in the instantaneous eigenstate of the Hamiltonian,[1] allowing stable, well-controlled mode evolution. When the modulation rate increases, however, the evolution departs from the adiabatic path, giving rise to nonadiabatic transitions such as Landau–Zener tunneling[2] in two-level systems, where the transition probability depends sensitively on the temporal sweep rate through an avoided crossing. Metamaterials have traditionally relied on static structures, key advances span optical metasurfaces for wavefront control,[3–6] bulk optical metamaterials enabling negative refraction and cloaking,[7–9] and resonant EM functionalities such as transparency and absorption,[10,11] alongside related progress in acoustic,[12–14] active/Willis-type,[15,16] and elastic platforms.[17,18] Building on these developments, temporally modulated systems now recently allow temporal modulations comparable to the wave oscillation period, opening access to new dynamic regimes of wave manipulation. Such systems have revealed rich phenomena including nonreciprocal propagation,[19] enhanced nonlinearities,[20–22] broadband frequency conversion,[23] and temporal analogues of spatial interference such as diffraction in time.[24] They also provide new routes for parametric amplification and time-dependent control of energy exchange.[25–28]

In parallel, non-Hermitian physics—particularly parity–time ($\mathscr{P}\mathscr{J}$) symmetry—has revealed how spatially balanced gain and loss can reshape modal spectra and direct energy flow. $\mathscr{P}\mathscr{J}$-symmetric systems have demonstrated selective amplification and mode conversion,[29–35] showing that the spatial gain–loss distribution governs competition between modes. However, most realizations remain static in time, limiting their ability to control when and how transitions between eigenmodes occur. Embedding $\mathscr{P}\mathscr{J}$ symmetry into a time-varying framework offers a new degree of freedom: spatial gain–loss contrast

*Centre for Metamaterial Research and Innovation, Department of Physics and Astronomy, University of Exeter, UK. E-mail: j.li13@exeter.ac.uk*

defines the stability and rate of amplification, while temporal modulation dictates the trajectory of modal evolution.

Here we introduce a spatiotemporal gain–loss framework that achieves *eigenmode steering* in coupled acoustic Helmholtz resonators. The total acoustic energy remains conserved through a *cross-coupled gain–loss coefficient* that links the gain of one resonator to the intensity of its partner, producing nonlinear feedback that drives the system toward fixed-point solutions corresponding to the eigenmodes of an effective non-Hermitian Hamiltonian. The eigenmode associated with the eigenvalue having the largest imaginary part naturally emerges as the attractor, realizing a deterministic form of *eigenmode steering*. By tailoring the spatial distribution of gain and loss, the eigenvalue spectrum and attractor landscape can be engineered, while temporal modulation governs transitions between eigenmodes. We further show that introducing controlled *spatiotemporal perturbations* enables transitions that would otherwise be symmetry-forbidden, providing an additional lever for accelerating convergence and controlling modal pathways. Through a $\mathscr{P}\mathscr{J}$-symmetric implementation, we demonstrate controlled switching between mode steering and Rabi-like oscillations, and programmable cyclic energy routing across multiple resonators. This establishes spatiotemporal gain–loss engineering as a general framework for reconfigurable acoustic manipulation, time-varying metamaterials, and analog information processing.

## 2 Results and discussions

### 2.1 Dimer model for eigenmode steering

Resonant systems support discrete eigenmodes whose amplitudes evolve under the combined effects of coupling and dissipation. To expose the basic mechanism of *eigenmode steering*, we begin with the simplest case—a dimer of two coupled resonators—in which the gain–loss distribution is programmed to guide the system toward a target eigenmode. We cast the coupled-resonator dynamics in Hamiltonian form to unify coupling, gain, and loss and to make explicit the state-dependent structure of the dynamics. The Hamiltonian is nonlinear because its gain–loss terms imaginary parts of the diagonal elements in eqn (2), depends on the instantaneous modal intensities. Physically, realizing these intensity-dependent gain/loss rates requires a closed-loop mechanism that both senses the resonator state and actuates gain or damping accordingly. In our acoustic implementation, this is achieved by extracting the complex envelopes $\psi_{a,b}$ from measured pressures, and programs the corresponding active-wall gain/loss, as detailed below.

The dynamics are described by the coupled-mode equation

$$i\frac{\mathrm{d}}{\mathrm{d}t}\begin{pmatrix}\psi_a\\ \psi_b\end{pmatrix} = H\begin{pmatrix}\psi_a\\ \psi_b\end{pmatrix}, \tag{1}$$

with the nonlinear Hamiltonian

$$H = \frac{1}{2}\begin{pmatrix} ig\frac{|\psi_b|^2}{E} & -\frac{\kappa}{2} \\ -\frac{\kappa}{2} & -ig\frac{|\psi_a|^2}{E}\end{pmatrix}, \tag{2}$$

where $\psi_a$ and $\psi_b$ are the complex envelopes of modes $a$ and $b$, $\kappa$ is the coupling coefficient, and $g$ is the *cross-coupled gain–loss coefficient*. This coefficient implements a nonlinear inter-site feedback: the gain (loss) experienced by one resonator depends on the intensity of its coupled partner. For $g > 0$, mode $a$ experiences gain $\propto |\psi_b|^2$, while mode $b$ experiences loss $\propto |\psi_a|^2$. Although these terms render the system non-Hermitian, their cross-coupled form ensures that the total energy.

$$E = |\psi_a|^2 + |\psi_b|^2$$

remains a constant of motion (see SI for derivation and extension to non-identical resonators). This nonlinearity provides a natural saturation mechanism that prevents unbounded growth or decay, enabling sustainable eigenmode steering. The normalization by $E$ in eqn (2) also guarantees scale invariance.

Such a nonlinear dimer can be implemented acoustically using two coupled Helmholtz resonators operating near a carrier frequency, *e.g.* chosen as $\omega/2\pi \approx 800$ Hz. A uniform rescaling of the Helmholtz resonators (cavity and neck) shifts the resonance (and thus the carrier) frequency, providing a direct way to move the operating band. If the coupling bridge is also scaled accordingly, the coupling and gain rates rescale in the same way, so the mode-steering dynamics remain the same up to an overall change of timescale. Since the pressure fields oscillate predominantly at this frequency, each resonator is represented by a slowly varying complex envelope $\psi_{a,b}$ extracted from the analytic pressure signal

$$\psi_{a,b}\mathrm{e}^{-i\omega t} = p_{a,b} + i\mathscr{H}[p_{a,b}],$$

where $p_{a,b}$ are the measured pressures and $\mathscr{H}[p_{a,b}]$ their Hilbert transforms, approximated under the narrowband condition as $\mathscr{H}[p_{a,b}] \approx -\omega\int p_{a,b}\mathrm{d}t$. This envelope description connects the data to eqn (1) and justifies removing common diagonal terms in $H$, since the model now governs slowly varying envelopes rather than rapidly oscillating carriers.

Inter-resonator coupling $\kappa$ arises from the connecting bridge (hollow tube), where a longer bridge leads to weaker coupling, while the cross-coupled gain–loss action is introduced through time-varying wall conductance $\Gamma_{a,b}$ at the upper cavity boundaries, following $\Gamma_{a,b} \propto \mp g|\psi_{b,a}|^2$ (Fig. 1(a)). Such an active wall boundary is able to generate a non-zero wall velocity from a previously zero value corresponding to a rigid (hard) boundary, *i.e.*, a finite $\Gamma$ through $v = \Gamma p$ at the cavity wall. Positive and negative $\Gamma$ correspond to acoustic loss (orange) and gain (green), implemented numerically *via* impedance boundary conditions or experimentally *via* feedback loops linking microphones and speakers on the cavity walls.[36,37] Two-dimensional finite-element simulations (COMSOL Multiphysics) determine $\kappa = 2\pi \times 163$ Hz and $g = \pm 2\pi \times 218$ Hz; For clarity, the parameters used here are selected for simulation convenience and faster convergence, and a demonstration of mode steering under more realistic experimental conditions is provided in the SI. Detailed geometric parameters and their design principle are also provided in there.

In principle, mode steering can be realized at higher frequencies higher than audible ones in this work by *entire*

 

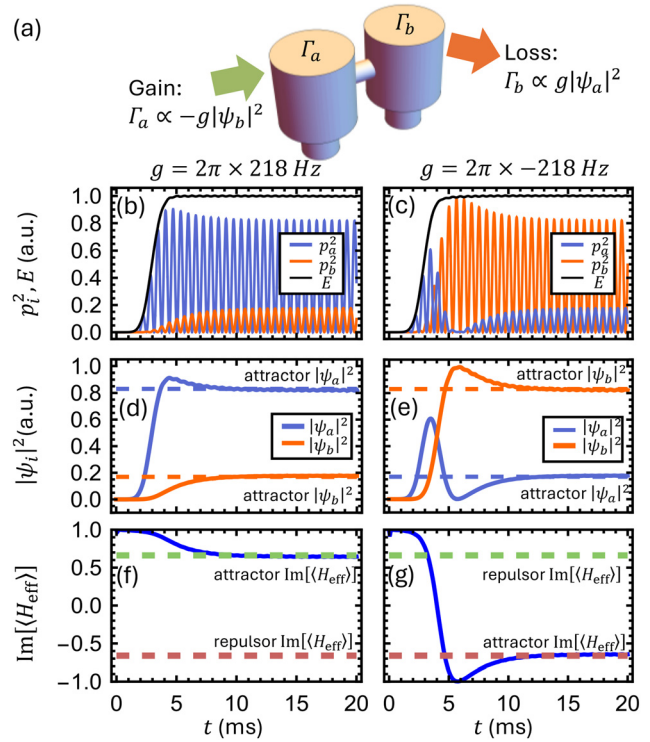


Fig. 1 (a) Schematic of the nonlinear acoustic dimer composed of two coupled Helmholtz resonators, where the *cross-coupled gain–loss coefficient* modulates wall conductance *via* $\Gamma_{a,b} \propto \mp g|\psi_{b,a}|^2$ and $v = \Gamma p$ at cavity wall. (b), (c) Simulated squared pressures $p_i^2$ and total energy $E$, and (d), (e) squared envelope amplitudes $|\psi_i|^2$, for (b), (d) $g = 2\pi \times 218$ Hz and (c), (e) $g = -2\pi \times 218$ Hz. Positive $g$ concentrates energy in resonator $a$, while negative $g$ favors resonator $b$, consistent with the attractor eigenmodes predicted by the effective Hamiltonian. Dashed horizontal lines denote steady-state fixed points. (f), (g) Projection metric $\mathrm{Im}[\langle\psi|H_{\mathrm{eff}}|\psi\rangle]$ for the simulated field (solid) and the attractor/repulsor eigenvectors of $H_{\mathrm{eff}}$ (dashed), confirming convergence to the corresponding eigenmode after the transient.

geometry, including the connecting bridge. In practice, however, increased viscous and resonant losses, together with fabrication limits such as surface roughness and tolerance in narrow coupling channels, constrain performance. In this case, we will need these additional losses compensated by additional feedback gain and the mode-steering behavior remains achievable.

Fig. 1(b)–(e) present the simulated squared pressures ${p_{a,b}}^2$ and corresponding complex evelope amplitudes $|\psi_{a,b}|^2$ for $g = \pm 2\pi \times 218$ Hz. Within approximately 5 ms after energy injection through the neck of resonator $a$, the system evolves toward distinct attractor states: for $g > 0$ energy concentrates in resonator $a$, whereas for $g < 0$ it localizes in resonator $b$. The total energy $E = |\psi_a|^2 + |\psi_b|^2$, shown in black, remains constant after the transient, confirming that the cross-coupled gain–loss feedback provides a saturation mechanism that sustains stable eigenmode steering without the exponential divergence typical of conventional gain systems.

The sustained convergence in Fig. 1 shows that the system evolves toward a unique modal state—*eigenmode steering*. Interestingly, one may note a conceptual parallel with wavefunction collapse in quantum mechanics, where nonlinear and irreversible dynamics guide a system toward an eigenstate of a measurement operator. Unlike the probabilistic nature of quantum collapse, the present system exhibits deterministic convergence through nonlinear eigenmode steering. We emphasize that this analogy is only meant to highlight a qualitative similarity, as both involve dynamics that can be engineered to select a preferred eigenmode through non-Hermitian mechanisms. On the other hand, the deterministic dynamics does resemble a post-selected trajectory associated with a probabilistic quantum wavefunction collapse. To describe this process, we introduce a linear *effective Hamiltonian* capturing the dominant modal dynamics:

$$H_{\mathrm{eff}} = \frac{1}{2}\begin{pmatrix} i\frac{g}{2} & -\frac{\kappa}{2} \\ -\frac{\kappa}{2} & -i\frac{g}{2} \end{pmatrix}. \tag{3}$$

The nonlinear Hamiltonian in eqn (2) decomposes as $H = H_{\mathrm{eff}} - iGI_2$, where $G = g(|\psi_a|^2 - |\psi_b|^2)/(4E)$ is a common nonlinear gain–loss term and $I_2$ is the $2 \times 2$ identity. Thus $H_{\mathrm{eff}}$ fixes the modal structure and eigenvalue spectrum, while $GI_2$ regulates the overall amplitude to conserve total energy. As detailed in SI S4, instantaneous eigenfrequency analysis reveals that nonlinear feedback dynamically suppresses net amplification, leading to a stable steady state.

Working in the eigenbasis of $H_{\mathrm{eff}}$, writing $(\psi_a, \psi_b) = a_1\psi_1 + a_2\psi_2$ with eigenvalues $\lambda_{1,2} = \pm\frac{1}{4}\sqrt{\kappa^2 - g^2}$, we obtain

$$\frac{\mathrm{d}}{\mathrm{d}t}\ln\left(\frac{a_1}{a_2}\right) = -i(\lambda_1 - \lambda_2), \tag{4}$$

so that $a_1/a_2 \propto e^{-i(\lambda_1-\lambda_2)t}$. The magnitude ratio grows or decays exponentially with rate $\mathrm{Im}[\lambda_1 - \lambda_2]$, driving the system toward the eigenmode with the larger imaginary part of eigenvalue (the *attractor*), while the other acts as a *repulsor*. For the present parameters, the attractor eigenmodes are $\psi_+ = \{0.91, 0.41i\}$ for $g = 2\pi \times 218$ Hz and $\psi_- = \{0.41i, 0.91\}$ for $g = -2\pi \times 218$ Hz. After the transient ($\sim$5 ms), the simulated steady-state intensities $\{|\psi_a|^2, |\psi_b|^2\} = \{0.83, 0.17\}$ and $\{0.17, 0.83\}$ (dashed lines in Fig. 1(d and e)) agree with these predictions. The projection metric $\mathrm{Im}[\langle\psi|H_{\mathrm{eff}}|\psi\rangle]$ in Fig. 1(f and g) further verifies steering onto the attractor branch—the upper band for $g > 0$ and the lower band for $g < 0$ —confirming deterministic eigenmode steering.

From a complementary perspective, the nonlinear dynamics can be viewed as arising from the linear non-Hermitian evolution with Hamiltonian in eqn (3) together with a normalization constraint that enforces energy conservation. Detailed derivation is included in SI S5. In this sense, the nonlinear term acts as a designed feedback that preserves the norm, making the effective Hamiltonian description not merely a perturbative approximation but an exact representation of the dynamics even during large excursions and transient evolution. This viewpoint explains why the stability and attractor structure inferred from the eigenvalue spectrum remain valid beyond the small perturbation regime unlike general nonlinear systems.

### 2.2 Attractor dynamics *vs.* Rabi-type oscillation

Having established eigenmode steering *via* spatial gain–loss distribution, we now introduce temporal control by modulating the gain–loss coefficient in time. As shown in Fig. 2(b), $g(t)$ alternates periodically between $+g_0$ and $-g_0$ (with $g_0 = 2\pi \times 218$ Hz), connected by 5 ms linear ramps. This creates a sequence of temporal boundaries that steer the system in real time between the two attractor eigenmodes of $H_{\text{eff}}$. The simulated intensities $|\psi_{a,b}|^2$ in Fig. 2(c) capture this evolution: following each reversal of $g(t)$, the system transitions from $\psi_+$ to $\psi_-$ (or *vice versa*), completing a full cycle of time-dependent eigenmode steering. When the modulation depth is reduced to $g_0 = 2\pi \times 91$ Hz, the system no longer converges after each switch but instead exhibits sustained Rabi-like oscillations between the two modes. The measured oscillation frequency ($\sim 2\pi \times 71$ Hz) agrees well with the beating frequency predicted by the linearized model ($\lambda_+ - \lambda_- = \frac{1}{2}\sqrt{\kappa^2 - g^2} = 2\pi \times 68$ Hz), confirming that the dynamics originate from the $\mathscr{PJ}$-symmetric phase.

This behavior originates from the $\mathscr{PJ}$ symmetry of $H_{\text{eff}}$, which satisfies $\mathscr{PJ}\, H_{\text{eff}} = H_{\text{eff}}\, \mathscr{PJ}$ with

$$\mathcal{P} = \begin{pmatrix} 0 & 1 \\ 1 & 0 \end{pmatrix}, \qquad \mathscr{T}: \text{complex conjugation}.$$

The symmetry divides parameter space into two regimes separated by an exceptional point (EP) at $|g_0| = \kappa = 2\pi \times 163$ Hz. As shown in Fig. 2(a), the eigenvalues are complex conjugates in the $\mathscr{PJ}$-broken phase ($|g_0| > \kappa$) and purely real in the $\mathscr{PJ}$-symmetric phase ($|g_0| < \kappa$). Eqn (4) shows that the modal amplitude ratio is driven by the eigenvalue separation:

$$\frac{d}{dt}\ln\left(\frac{a_1}{a_2}\right) = -i(\lambda_1 - \lambda_2).$$

When $\mathrm{Im}[\lambda_1 - \lambda_2] > 0$ (broken phase), $|a_1/a_2|$ grows exponentially, yielding deterministic steering to the dominant eigenmode. The imaginary gap $\mathrm{Im}[\lambda_1 - \lambda_2] = \frac{1}{2}\sqrt{g^2 - \kappa^2}$ sets the characteristic convergence time $\tau_c \sim 1/\mathrm{Im}[\lambda_1 - \lambda_2]$, providing a universal indicator of modal stability and converging rate. Where this convergence is evaluated as 2.2 ms in Fig. 1 which agrees to the decay time around 5 ms. When $\mathrm{Im}[\lambda_1 - \lambda_2] = 0$ (symmetric phase), both modes remain balanced, producing sustained Rabi-like oscillations. We note that the temporal modulation period is chosen to be 60 ms to ensure complete mode steering; in principle, it can be reduced toward the characteristic convergence timescale $\tau_c \approx 2.2$ ms, provided the steering process remains complete. For example, a lower $\kappa$ resulting from a longer connecting bridge reduces the steering threshold and decreases the convergence time, leading to faster mode steering and faster temporal modulation as long as the separation remains much smaller than the acoustic wavelength. Additionally, increasing the gain can also accelerate convergence, provided the physical implementation allows sufficiently large gain.

Unlike conventional $\mathscr{PJ}$-symmetric platforms where total energy diverges or decays, the present cross-coupled, energy-conserving framework yields sustainable, bounded dynamics in both regimes and enables smooth cascading across successive stages of time-dependent eigenmode steering. Moreover, the eigenvalue spectrum of $H_{\text{eff}}$ directly identifies attractor and repulsor modes without a separate Jacobian analysis, offering a global, predictive view of stability.

As a side note, realistic implementations of the dimer introduce finite signal-processing latency arising from analytic-signal extraction and possible bandpass filtering. Simulations including these delays show that, although transient overshoot may increase, the qualitative features of mode steering remain unchanged, confirming the robustness of the dynamics (see SI).

Moreover, although the two-mode model predicts dynamical stability, practical implementations may introduce additional instability channels, including excitation of higher-order modes, unintended broadband feedback, feedback jitter (*i.e.*, uncertainty in loop timing), and fluctuations in the feedback gain. These effects can be mitigated through bandpass filtering, which suppresses higher-order modes and unintended broadband feedback, and through digital feedback control, which stabilizes the loop timing and regulates gain fluctuations, thereby ensuring operation within the stability regime consistent with the model.

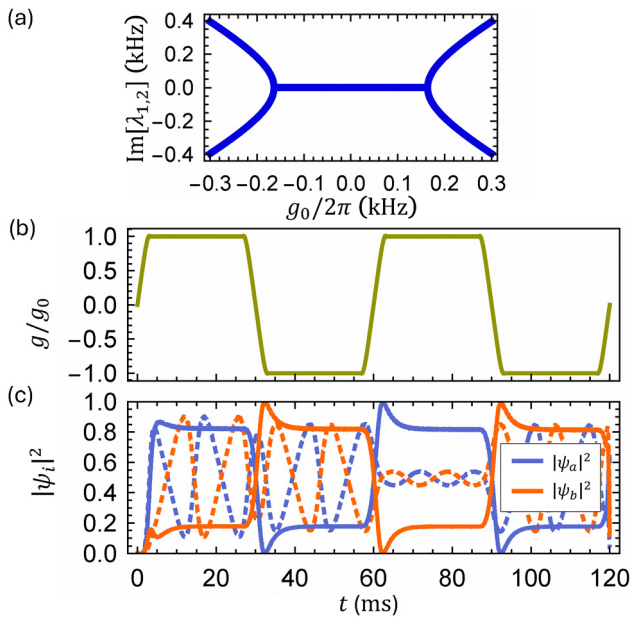


Fig. 2 (a) Imaginary parts $\mathrm{Im}[\lambda_{1,2}]$ of $H_{\text{eff}}$ showing $\mathscr{PJ}$-symmetric and $\mathscr{PJ}$-broken phases separated by the exceptional point $|g_0| = \kappa = 2\pi \times 163$ Hz. (b) Temporal modulation of $g$ between $\pm g_0$ for time-dependent eigenmode steering. (c) Simulated $|\psi_i|^2$ for $g_0 = 2\pi \times 218$ Hz (solid, broken phase) and $g_0 = 2\pi \times 91$ Hz (dashed, symmetric phase). In the broken phase, the system converges to fixed-point eigenmodes (as in Fig. 1); in the symmetric phase it exhibits sustained oscillations.

### 2.3 Trimer model: cyclic eigenmode steering and energy routing

We now extend from two to three coupled resonators to demonstrate how spatiotemporal control routes energy across multiple targets. This trimer is the minimal network supporting

sequential redistribution and symmetry-mediated transitions. Its dynamics obey

$$i\frac{\mathrm{d}}{\mathrm{d}t}\begin{pmatrix}\psi_a\\ \psi_b\\ \psi_c\end{pmatrix} = H\begin{pmatrix}\psi_a\\ \psi_b\\ \psi_c\end{pmatrix}, \tag{5}$$

where $H$ contains Hermitian coupling and nonlinear non-Hermitian feedback. For clarity, we consider three identical resonators with identical bridges. We decompose $H = H_3 + H_{\mathrm{NL}}$, where

$$H_3 = \frac{1}{2}\begin{pmatrix}0 & -\kappa/2 & -\kappa/2\\ -\kappa/2 & 0 & -\kappa/2\\ -\kappa/2 & -\kappa/2 & 0\end{pmatrix}, \tag{6}$$

is the symmetric Hermitian coupling with the common diagonal absorbed into the carrier, consistent with the envelope description. The nonlinear non-Hermitian term, implementing cross-coupled gain–loss feedback, is diagonal:

$$H_{\mathrm{NL}} = \frac{i}{2E}\mathrm{diag}(g_{ab}|\psi_b|^2 + g_{ac}|\psi_c|^2, g_{bc}|\psi_c|^2 + g_{ba}|\psi_a|^2,\ g_{ca}|\psi_a|^2 + g_{cb}|\psi_b|^2), \tag{7}$$

where $E = |\psi_a|^2 + |\psi_b|^2 + |\psi_c|^2$ and $g_{ij} = g_i - g_j$ are cross-site gain–loss contrasts derived from the site-based *cross-coupled gain–loss coefficients* $g_i$ assigned to $i \in \{a, b, c\}$. Only differences $g_{ij}$ carry physical meaning; this construction ensures total energy conservation (see SI).

Following the dimer, we introduce an effective Hamiltonian for modal dynamics:

$$H_{\mathrm{eff}} = \frac{1}{2}\begin{pmatrix}ig_a & -\kappa/2 & -\kappa/2\\ -\kappa/2 & ig_b & -\kappa/2\\ -\kappa/2 & -\kappa/2 & ig_c\end{pmatrix}. \tag{8}$$

The full Hamiltonian takes $H = H_{\mathrm{eff}} - iG_3I_3$, with

$$G_3 = \frac{1}{2E}(g_a|\psi_a|^2 + g_b|\psi_b|^2 + g_c|\psi_c|^2),$$

and $I_3$ the identity. Here, $H_{\mathrm{eff}}$ sets the modal structure, while $G_3$ regulates amplitude to conserve energy. As in the dimer, for any two eigenmodes $\psi_i$, $\psi_j$,

$$\frac{a_i}{a_j} \propto e^{-i(\lambda_i - \lambda_j)t},$$

so the eigenmode associated with the eigenvalue having the largest imaginary part dominates (given nonzero initial projection). Thus the direction of energy routing and the steady-state distribution are programmed by the spatiotemporal schedule of $g_a$, $g_b$, and $g_c$.

Fig. 3 demonstrates programmable cyclic *eigenmode steering* and energy routing. As shown in Fig. 3(a), the site coefficients $\{g_a, g_b, g_c\}$ are modulated in 60-ms intervals to realize the sequence $a \to b \to c \to a$. During each interval, one cavity is activated with gain ($g_i = g_0 > 0$), while the others remain neutral

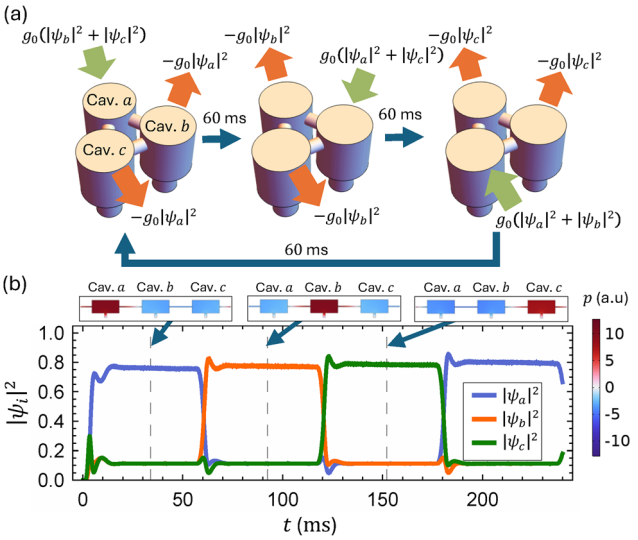


Fig. 3 (a) Schematic of energy routing in the nonlinear acoustic trimer of eqn (5). Cyclic spatiotemporal modulation applies a relative gain $g_0$ sequentially for 60 ms: $(g_a, g_b, g_c) = (g_0, 0, 0) \to (0, g_0, 0) \to (0, 0, g_0) \to \cdots$, steering modal dominance $a \to b \to c \to \cdots$. (b) Simulated $|\psi_{a,b,c}|^2$ showing periodic convergence to distinct fixed points during each step. Representative pressure-field distributions are shown in inset for each interval.

($g_j = g_k = 0$). The arrows and accompanying formulas in Fig. 3(a) follow directly from the nonlinear feedback term in eqn (7), where the local contribution for each cavity takes the form $\frac{i}{2E}\left(g_{ij}|\psi_j|^2 + g_{ik}|\psi_k|^2\right)$ with $g_{ij} = g_i - g_j$. A positive imaginary value (green arrow) represents gain fed by neighbouring intensities, while a negative value (orange arrow) denotes the corresponding loss channel. For example, when $(g_a, g_b, g_c) = (g_0, 0, 0)$, cavity $a$ acquires gain $\propto |\psi_b|^2 + |\psi_c|^2$, whereas $b$ and $c$ experience equal losses $\propto |\psi_a|^2$. As the active gain site switches sequentially to $b$ and then to $c$, the dominant eigenmode of $H_{\mathrm{eff}}$ shifts accordingly, guiding energy around a closed loop through a time-dependent attractor landscape. The simulated intensities in Fig. 3(b) confirm precise cyclic routing using the same parameters as the dimer ($g_0 = 2\pi \times 218$ Hz, $\kappa = 2\pi \times 163$ Hz). For instance, $(g_a, g_b, g_c) = (g_0, 0, 0)$ yields the dominating eigenmode $\psi_1 = \{-1.47\text{–}2.03i, 1, 1\}$ (eigenvector of eqn (8) having eigenvalue of the largest imaginary part) with maximal amplitude in cavity $a$. The observed cyclic switching of modal dominance demonstrates deterministic routing *via* programmed spatiotemporal gain–loss modulation.

### 2.4 Overcoming symmetry-forbidden transitions *via* spatiotemporal perturbation

We now demonstrate assisted *eigenmode steering* for a transition that is *symmetry-forbidden* under ideal conditions. We switch the site schedule from a single-cavity preference $(g_a, g_b, g_c) = (g_0, 0, 0)$ to a dual-cavity configuration $(g_a, g_b, g_c) = (0, g_0, g_0)$, aiming to redistribute energy from resonator $a$ into equal amplitudes in resonators $b$ and $c$ (Fig. 4(a)(i, ii)). The target attractor eigenmode of the dual-cavity configuration is $\psi_1' = \{0, 1, -1\}$ (largest

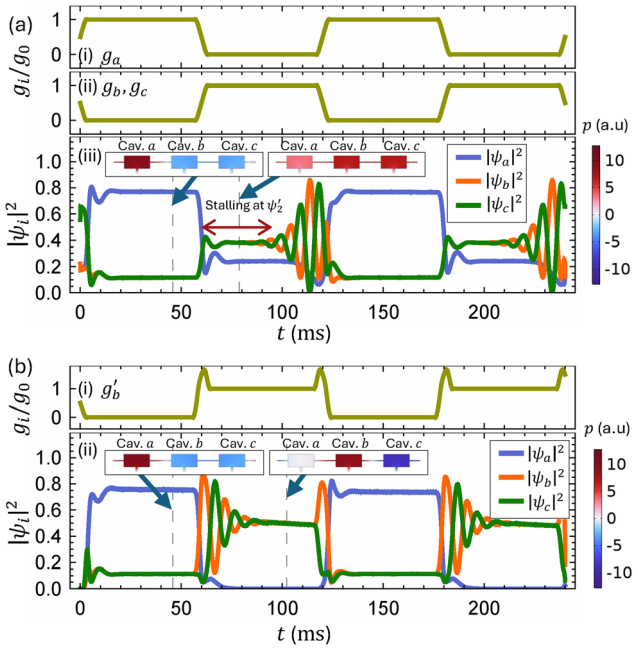


Fig. 4 (a) Spatiotemporal profile for redistributing total energy to cavities $b$ and $c$. (i) Modulation schemes for $g_a$, (ii) for $g_b$, $g_c$ with symmetric modulation ($g_b = g_c$). (iii) Simulated $|\psi_{a,b,c}|^2$. Energy concentrates in cavity $a$ during the first 60 ms (matching Fig. 3(b)) but fails to redistribute to $b$ and $c$ during $60 < t < 120$ ms, unable to reach the target eigenmode $\psi_1' = \{0, 1, -1\}$. (b) Successful redistribution using a *spatiotemporal perturbation* applied as a transient modification $g_b'(t)$ in (i). (ii) Simulated $|\psi_{a,b,c}|^2$ show that this perturbation enables the previously symmetry-forbidden transition, with convergence to $\psi_1'$ at $t \simeq 100$ ms. Pressure field patterns are sampled and shown for each interval.

imaginary part of eigenvalue), which suppresses cavity $a$ while establishing equal and opposite phases in $b$ and $c$.

Full-wave simulations in Fig. 4(a)(iii) show that this transition does not occur spontaneously. After the gain reconfiguration at $t$ = 60 ms, the system becomes trapped in an intermediate state $\psi_2' = \{0.47 + 0.64i, 1, 1\}$ instead of collapsing to the antisymmetric target. Energy partially transfers from $a$ (blue) to $b$ and $c$ (orange/green), but cavity $a$ retains significant amplitude. This trapping arises from a parity mismatch: the initial eigenmode $\psi_1$ has $b$ and $c$ in phase, whereas the target $\psi_1'$ requires them out of phase. Because $(0, g_0, g_0)$ is parity-symmetric, it cannot couple even- and odd-parity modes; the transition is therefore symmetry-forbidden in the ideal, noiseless system.

To enable and accelerate the transition, we introduce a controlled *spatiotemporal perturbation*—a transient modification to $g_b(t)$ (leaving $g_a(t)$ unperturbed), as in Fig. 4(b)(i). This momentarily breaks the $b$–$c$ symmetry at the switching points, lifting the parity constraint and directing convergence to the target eigenmode. Fig. 4(b)(ii) shows rapid convergence to $\psi_1'$ within $t \approx 100$ ms, achieving complete redistribution: resonator $a$ is fully suppressed while $b$ and $c$ are equally amplified with opposite phase. A more rigorous formulation based on a symmetry selection rule is provided in SI S7, where we show that symmetry forbids transitions between attractors unless explicitly broken and derive the corresponding perturbative scaling.

Thus temporal modulation governs not only eigenmode selection but also the transition pathway; small, designed spatiotemporal perturbations can dramatically enhance convergence rates by removing symmetry bottlenecks. In this framework, the spatial profile defines the target eigenmodes, while temporal perturbations program the kinetics of steering toward them.

Finally, we note that the steering dynamics discussed above naturally extend beyond the minimal dimer and trimer settings and can be generalized to larger coupled-cavity networks. A constructive parameter-selection procedure is provided in the SI, where the off-diagonal couplings are treated as free design variables and the diagonal detuning/gain terms are determined accordingly to realize a prescribed eigenmode. More broadly, increasing the cavity number $n$ increases the number of tunable couplings, providing additional degrees of freedom to engineer the eigenvalue separations and thereby tune the characteristic steering time.

## 3 Conclusion

We have established a spatiotemporal gain–loss framework that enables *eigenmode steering* in coupled acoustic resonators. The dynamics are governed by a nonlinear Hamiltonian featuring a *cross-coupled gain–loss coefficient*, which enforces total energy conservation while guiding the system toward fixed points corresponding to the eigenvectors of an effective non-Hermitian Hamiltonian. Within this framework, the eigenmode associated with the eigenvalue having the largest imaginary part naturally emerges as the attractor, realizing a deterministic form of *eigenmode steering*.

Time-dependent modulation of the gain–loss coefficient reveals two distinct regimes divided by the exceptional point: the $\mathscr{PJ}$-broken phase, exhibiting stable eigenmode convergence, and the $\mathscr{PJ}$-symmetric phase, characterized by sustained Rabi-like oscillations. Extending the concept to a trimer system demonstrates programmable and cyclic *eigenmode steering* across multiple resonators. Moreover, introducing controlled *spatiotemporal perturbations* enables transitions that are otherwise *symmetry-forbidden*, providing an additional temporal degree of control that accelerates convergence and lifts symmetry constraints.

Validated by full-wave simulations of coupled Helmholtz resonators, this framework unifies nonlinear feedback, $\mathscr{PJ}$ symmetry, and time-varying control into a single platform for sustainable and reconfigurable acoustic manipulation. It opens pathways toward adaptive noise control, programmable metamaterials, and analog information processing, and offers broader insight into how spatiotemporal gain–loss engineering can shape wave dynamics in non-Hermitian and energy-conserving systems.

## Conflicts of interest

There are no conflicts to declare.

## Data availability

Supplementary information (SI): includes the complete simulation setup and parameters required to reproduce the results. See DOI: https://doi.org/10.1039/d5mh02136g.

The simulation data supporting this study can be obtained from the corresponding author upon reasonable request.

## Acknowledgements

The authors acknowledge financial support from the EPSRC *via* the META4D Programme Grant (No. EP/Y015673/1). The authors also thank Prof. Simon Horsley for insightful and fruitful discussions. For the purpose of open access, the author has applied a Creative Commons Attribution (CC BY) licence to any Author Accepted Manuscript version arising from this submission.

## References

1 M. Born and V. Fock, *Z. Med. Phys.*, 1928, **51**, 165–180.
2 C. Wittig, *J. Phys. Chem. B*, 2005, **109**, 8428–8430.
3 N. Yu, P. Genevet, M. A. Kats, F. Aieta, J.-P. Tetienne, F. Capasso and Z. Gaburro, *Science*, 2011, **334**, 333–337.
4 G. Zheng, H. Mühlenbernd, M. Kenney, G. Li, T. Zentgraf and S. Zhang, *Nat. Nanotechnol.*, 2015, **10**, 308–312.
5 S. Wang, P.-C. Wu, V.-C. Su, Y.-C. Lai, M.-K. Chen, H.-Y. Kuo, B.-H. Chen, Y.-H. Chen, T.-T. Huang, J.-H. Wang, R.-M. Lin, C.-H. Kuan, T. Li, Z. Wang, S. Zhu and D. P. Tsai, *Nat. Nanotechnol.*, 2018, **13**, 227–232.
6 J. Zhou, S. Liu, H. Qian, Y. Li, H. Luo, S. Wen, Z. Zhou, G. Guo, B. Shi and Z. Liu, *Sci. Adv.*, 2020, **6**, eabc4385.
7 C. M. Soukoulis, S. Linden and M. Wegener, *Science*, 2007, **315**, 47–49.
8 J. B. Pendry, *Phys. Rev. Lett.*, 2000, **85**, 3966–3969.
9 X. Ni, Z. J. Wong, M. Mrejen, Y. Wang and X. Zhang, *Science*, 2015, **349**, 1310–1314.
10 S. Zhang, D. A. Genov, Y. Wang, M. Liu and X. Zhang, *Phys. Rev. Lett.*, 2008, **101**, 047401.
11 Q. Li, Z. Zhang, L. Qi, Q. Liao, Z. Kang and Y. Zhang, *Adv. Sci.*, 2019, **6**, 1801057.
12 Y. Li, B. Liang, Z.-M. Gu, X.-Y. Zou and J.-C. Cheng, *Sci. Rep.*, 2013, **3**, 2546.
13 J. Li and C. T. Chan, *Phys. Rev. E:Stat., Nonlinear, Soft Matter Phys.*, 2004, **70**, 055602(R).
14 B.-I. Popa, Y. Zhai and H.-S. Kwon, *Nat. Commun.*, 2018, **9**, 5299.
15 L. Wu, X. Qiu and Y. Guo, *Appl. Acoust.*, 2014, **81**, 40–46.
16 Y. Xie, W. Wang, H. Chen, A. Konneker, B.-I. Popa and S. A. Cummer, *Nat. Commun.*, 2014, **5**, 5553.
17 M. Yan, J. Lu, F. Li, W. Deng, X. Huang, J. Ma and Z. Liu, *Nat. Mater.*, 2018, **17**, 993–998.
18 R. Zhu, X. N. Liu, G. K. Hu, C. T. Sun and G. L. Huang, *J. Sound Vib.*, 2014, **333**, 2759–2773.
19 X. Guo, Y. Ding, Y. Duan and X. Ni, *Light: Sci. Appl.*, 2019, **8**, 123.
20 S. Taravati, *Phys. Rev. Appl.*, 2018, **9**, 064012.
21 N. A. Estep, D. L. Sounas, J. Soric and A. Alù, *Nat. Phys.*, 2014, **10**, 923–927.
22 R. Tirole, S. Vezzoli, D. Saxena, S. Yang, T. V. Raziman, E. Galiffi, S. A. Maier, J. B. Pendry and R. Sapienza, *Nat. Commun.*, 2024, **15**, 7752.
23 H. Moussa, G. Xu, S. Yin, E. Galiffi, Y. Ra'di and A. Alù, *Nat. Phys.*, 2023, **19**, 863–869.
24 R. Tirole, S. Vezzoli, E. Galiffi, I. Robertson, D. Maurice, B. Tilmann, S. A. Maier, J. B. Pendry and R. Sapienza, *Nat. Phys.*, 2023, **19**, 999–1004.
25 E. Galiffi, P. A. Huidobro and J. B. Pendry, *Phys. Rev. Lett.*, 2019, **123**, 206101.
26 J. B. Pendry, E. Galiffi and P. A. Huidobro, *J. Opt. Soc. Am. B*, 2021, **38**, 3360–3368.
27 Q. Yang, H. Hu, X. Li and Y. Luo, *Photonics Res.*, 2023, **11**, B125–B134.
28 T. T. Koutserimpas, A. Alù and R. Fleury, *Phys. Rev. A*, 2018, **97**, 013839.
29 C. M. Bender and S. Böttcher, *Phys. Rev. Lett.*, 1998, **80**, 5243–5246.
30 R. El-Ganainy, K. G. Makris, M. Khajavikhan, Z. H. Musslimani, S. Rotter and D. N. Christodoulides, *Nat. Phys.*, 2018, **14**, 11–19.
31 L. Feng, Z. J. Wong, R.-M. Ma, Y. Wang and X. Zhang, *Science*, 2014, **346**, 972–975.
32 H. Hodaei, M.-A. Miri, A. U. Hassan, W. E. Hayenga, M. Heinrich, D. N. Christodoulides and M. Khajavikhan, *Laser Photonics Rev.*, 2016, **10**, 494–499.
33 M. H. Teimourpour, M. Khajavikhan, D. N. Christodoulides and R. El-Ganainy, *Sci. Rep.*, 2017, **7**, 10756.
34 Q. Zhong, S. K. Özdemir, A. Eisfeld, A. Metelmann and R. El-Ganainy, *Phys. Rev. Appl.*, 2020, **13**, 014070.
35 X. Wen, H. K. Yip, C. Cho, J. Li and N. Park, *Phys. Rev. Lett.*, 2023, **130**, 176101.
36 C. Shen, X. Zhu, J. Li and S. A. Cummer, *Phys. Rev. B*, 2019, **100**, 054302.
37 M. Rupin, G. Lerosey, J. de Rosny and F. Lemoult, *New J. Phys.*, 2019, **21**, 093012.